PNAS

Main Manuscript for

Reconfiguration of brain-wide neural activity after early life adversity.

Taylor W. Uselman[1], Russell E. Jacobs[2,3], Elaine L Bearer[1,3]

[1] University of New Mexico Health Sciences Center, Albuquerque, NM 87131
[2] Zilkha Neurogenetic Institute, Keck School of Medicine of University of Southern California, Los Angeles, CA 90033
[3] California Institute of Technology, Pasadena, CA 91125

Corresponding Author: Elaine L. Bearer
Email: elaine.bearer@gmail.com; ebearer@salud.unm.edu

Author Contributions: T.W.U. performed research, contributed analytical tools, analyzed data and wrote the manuscript; R.E.J. designed and performed research, developed the imaging protocol, analyzed data and edited the manuscript; E.L.B. designed and performed research, analyzed data, wrote and edited the manuscript.

Competing Interest Statement: The authors declare no competing interests.

Classification: Biological Sciences (Major), Neuroscience (Minor).

Keywords: manganese-enhanced magnetic resonance imaging, brain states, neuroimaging, early life adversity, acute threat

This PDF file includes:

Main Text
Figures 1 to 6

Abstract

Early life adversity (ELA) predisposes individuals to physical and mental disorders lifelong. How ELA affects brain functions, leading to these vulnerabilities, is a mystery. To understand ELA's impacts, investigations into neural activity affected by ELA must go beyond localized areas toward simultaneous recordings from multiple widely distributed regions. Such studies will expose relative activity between regions and discover shifts in regional activity in response to different experiences. Here, we performed longitudinal manganese-enhanced magnetic resonance imaging (MEMRI) to measure brain-wide neural activity in ELA-exposed mice across a series of experiences in adulthood. To ascertain whether ELA resulted in atypical brain activity, results were compared to those of the standard mouse (Std). MEMRI captured activity in the freely moving home cage condition, and short- and long-term after acute exposure to TMT, an innate predator threat. Images were normalized and aligned then analyzed with statistical mapping and automated segmentation. We found that neural activity in the home cage was greater in ELA compared to Std in multiple striatal-pallidal and hypothalamic regions. Upon acute threat, neural activity in Std increased in these regions to become more similar to that in ELA, while new hyperactive responses in ELA emerged in the midbrain and hindbrain. Nine days after acute threat, heightened neural activity in ELA remained within locus coeruleus and increased within posterior amygdala, ventral hippocampus, and dorsomedial and ventromedial hypothalamus. These results reveal functional imbalances that arise between multiple brain-systems after ELA, which are dependent upon context and cumulative experiences into adulthood.

Significance Statement

Early life adversity (ELA) is a crucial determinant of adult health. Yet, the neurobiological basis for this association remains elusive. Neural activity differs within localized brain regions in rodents who experienced ELA, but how this localized activity contributes to overall brain states has hitherto been unknown. Here we used longitudinal manganese-enhanced MRI to reveal brain-wide activities altered by ELA. Computational analyses revealed widespread reconfiguration of segment-wise neural activity throughout the brain across a series of conditions: freely moving, experiencing threat or its aftermath. These brain state dynamics were unique to ELA. Reconfiguration of brain states after ELA, shown here for the first time, may explain vulnerability to mental and physical disorders after childhood adversity.

Main Text

Introduction

Early life adversity (ELA) poses risks for neuropsychiatric disorders, especially after a second traumatic event, such as a life-threatening experience (1-5). ELA's long-term consequences on global neural activity into adulthood could serve as a biological basis for poor outcomes (6-8). We are studying the brain states of adult mice who experienced early life adversity and how their dynamics progress from being in the home cage to short- and long-term after acute threat. To ascertain how a potentially normal mouse is affected by ELA into adulthood, we compared ELA-exposed mice to the standard mouse reared under generalized conditions (9, 10).

We invoked ELA in mice using a well-established paradigm: fragmented maternal care induced by limited bedding (11, 12). Most studies using preclinical paradigms focus on localized brain regions with invasive methods (13-27). Only a few have examined ELA's brain-wide consequences (28-31). Lacking are any studies that examine the brain-wide effects of threat in the adult previously exposed to ELA. Many questions remain that cannot be answered by localized techniques, such as whether brain-wide activity is changed in an adult who has experienced ELA, and whether activity in response to threat is also affected. To investigate these questions and overcome inherent limitations of other techniques, we employed longitudinal manganese-enhanced MRI (MEMRI) together with computational data-driven analysis.

Longitudinal MEMRI detects brain-wide activity before, during and after acute threat in awake freely moving mice (32, 33). Predator odor is a widely accepted paradigm for naturalistic innate threat in rodents (56-58). MEMRI does not require invasive or destructive procedures (33). Mn(II) is safe, even continuous infusion of low doses has minimal effects on behavior (33, 34). We chose to deliver Mn(II) via two single bolus injections in order to avoid surgical procedures required for continuous infusion and to allow for Mn(II) clearance between imaging sessions (32). Systemic Mn(II) distributes throughout the brain parenchyma (35), enters active neurons through voltage-gated calcium channels (36, 37) and accumulates in neurons in an activity-dependent manner (33, 38, 39). Regional accumulations of Mn(II) throughout the brain produce robust hyperintense MR signals with large effect sizes at 100 μm^3 resolution (32, 33, 35, 40-42). These signals represent a composite picture of regional neural activity occurring between the time of injection and imaging. Alignment of multiple MR images, collected repeatedly from large cohorts of individuals as they progress in parallel through a series of experiences, produces a dataset that enables extraction of statistically significant voxel-wise information about brain-wide activity over time, not possible with

most other techniques (32, 33, 43-54). Such processing is a well-accepted practice in human imaging that yields much useful information and is routinely repurposed for rodent imaging (51, 55-58). To ensure reliability and reproducibility, computational processing is verified and validated at each step. Thus, MEMRI can uniquely image enduring consequences of ELA on brain-wide activity in the adult and its dynamics in response to threat.

Here, we examine the consequences of ELA on adult brain-wide activity during normal home cage exploration in the adult and investigate how this activity changes in response to acute threat, short and long term, with data-driven and hypothesis-based analyses of MEMRI images captured longitudinally. Our alignments and computational processing pipeline were rigorously verified at every step. We validated Mn(II) dose by showing similar intensity measurements across all individuals. We verified that Mn(II) signal replicated neural activity detected by other methods by measuring intensities in circuits known to be involved in predator odor responses and by correlation of Mn(II)-dependent enhancements with c-fos expression. We used within- and between-group statistical parametric mapping and automated segmentation with our new *InVivo* mouse brain atlas to quantify relative activity within and between 101 segments brain-wide under each condition. We found that volumes of activities in multiple segments throughout the brain differed significantly between standard mice and those exposed to ELA undergoing the same experiential timeline.

Results

To witness neural activity in the home cage condition (HC) of adult mice who experienced ELA, and their responses to predator stress short- and long-term, we adapted our longitudinal imaging procedure (**Fig. 1A**) (32). We compared ELA mice (ELA, n = 12) to pool-weaned JAX-reared mice of the same strain (Standard, Std, n = 12) to determine whether brain-wide activity of adult mice who had experienced ELA differed from a phenotypically “normal” adult mouse.

Successful Replication of Behavioral Paradigms. To test whether our protocols for these two paradigms, fragmented care (ELA) and predator stress (TMT), faithfully reproduced previously reported behaviors (59-61), we compared videos of adult mice as they explored a custom arena (**Fig. 1B-D**). For the effect of ELA experience, we measured the time ELA mice spent in the light at baseline (BL) and compared that to Std mice. As expected, adult ELA mice spent 10% more time in the light at BL than Std, demonstrating a persisting effect of ELA experience in an unprovoked situation ($p < 0.05$ FDR, Cohen’s $d = 1.58$) (**Fig. 1B**). For the effect of TMT, we measured time spent in the light and compared between BL and TMT. As expected, TMT decreased time spent in the light in both ELA and Std mice by more than 20%, demonstrating an acute effect of TMT (p <

106 0.05 FDR, Cohen's d_{Std} = 2.29, d_{ELA} = 3.42). To assess mouse recovery from MR anesthesia before
107 being presented with TMT, we measured distance traveled in 1 min epochs and tracked
108 movements from the beginning of a 10 min exposure to TMT (**Fig. 1C-D**). During the first minute of
109 TMT-exposure, distance traveled was equal to or greater than that at BL. Motility then decreased
110 by 50% or more over the 10 min TMT-exposure period ($p < 0.05$, FDR). These data support the
111 contention that our procedures faithfully reproduced ELA and TMT paradigms, giving us confidence
112 in assigning behavioral characteristics to unknown brain-wide activity.
113
114 **Longitudinal Imaging.** Our MR imaging protocol captures 8 sequential images across 12
115 individuals for each group (ELA and Std), yielding a total of 192 raw images with >2 million voxels
116 each (**Fig. 1E**). To ensure no differences between groups were introduced by processing, all
117 images were processed as a batch through our semi-automated processing pipeline (32, 33). This
118 pipeline yielded a combined dataset of skull-stripped, intensity normalized and spatially aligned
119 images ready for statistical evaluation. Quality assurance considerations included reviewing
120 imaging parameters, performing SNR measurements to confirm similar Mn(II) doses, visualizing
121 modal scaling output in voxel-by-intensity histograms to monitor equivalent intensity normalization,
122 calculating Jaccard Similarity and Mutual Information Indices for alignment accuracy, and
123 determining that smoothing does not significantly change regional signal intensities. All images
124 reported here met our quality assurance standards (***SI Appendix*** **Fig. S1-2** and **Table S1**).
125
126 **Brain States in Mice Exposed to ELA**. To detect Mn(II)-enhancements in ELA mice across
127 conditions from the home cage (HC) to post-threat (TMT) to nine days after threat (D9), we
128 compared post-Mn(II) images for each condition to each mouse's respective pre-Mn(II) image using
129 voxel-wise statistical parametric mapping (SPM) (**Fig. 2**). SPM of images at HC revealed large
130 volumes of statistically significant signals in multiple brain regions identified by anatomy,
131 demonstrating that the unprovoked ELA brain was already highly active ($T = 2.72$, $p < 0.01$, cluster
132 corr.) (**Fig. 2A**). Larger volumes of SPM signal were seen within regions of the olfactory bulb,
133 striatum/pallidum, hypothalamus, hindbrain, and cerebellum, and smaller volumes within
134 subregions of hippocampus, amygdala, and hindbrain. Immediately after TMT, signals in these
135 regions were maintained or expanded in volume, with sizable increases in the mid- and hindbrain
136 (e.g., LC) (**Fig. 2B**). By D9, activity decreased overall in olfactory, hindbrain, and cerebellum, or
137 increased overall in hippocampus, amygdala, and midbrain (e.g., PAG) (**Fig. 2C**). Other subregions
138 also changed, such as a decrease of the volume of statistical signal in the lateral septum (LS) and
139 appearance of new signal in the paraventricular nucleus of the thalamus (PVT). Direct SPM paired
140 t-test comparisons between ELA post-Mn(II) images at each condition added to these findings from
141 activation volumes, to also identify statistical differences in signal intensities within many regions

142 across conditions (***SI Appendix* Fig. S3**). These findings indicate that ELA-exposed brains are
143 already highly active before a second provocation in adulthood, and that short- and long-term brain
144 responses to TMT have unique patterns of activity, with regions emerging or disappearing between
145 conditions.
146
147 **Magnitude of Signal Enhancements.** To determine whether differences in statistical maps
148 accurately represent intensity changes across conditions, and to test whether signal intensities
149 increase in response to TMT within expected regions, we measured and compared signal
150 intensities within 3 x 3 x 3 voxel regions of interest (ROI) between conditions (**Fig. 3A**, and ***SI***
151 ***Appendix* Tables S2** and **S3**). We selected these ROIs due to their involvement in predator odor
152 responses (62, 63), to determine the magnitude of intensity difference suggested by SPM. Our
153 previous, voxel-wise SPM of ELA images at HC and TMT revealed significantly enhanced signal
154 intensities after TMT in all four expected regions ($p<0.05$ cluster corr.). At HC, dlOB-DII and vlAON,
155 were already enhanced and only minimally changed across conditions. Region of interest (ROI)
156 measurements within these locations revealed that these SPM signals at HC represented large
157 signal differences over pre-Mn(II) (6.8%, dlOB-DII; 8.0%, vlAON) and large Cohen's D effect sizes
158 ($d = 1.6$, dlOB-DII; $d = 1.5$, vlAON; $p < 0.05$ FDR). In aOC and aCEA, SPM signals were minimal
159 at HC and increased from HC to TMT. These SPM signal changes were recapitulated in ROI
160 comparisons, with aOC and aCEA showing small magnitudes of signal enhancement over pre-
161 Mn(II) at HC (1.4 and 3.0%), and larger magnitudes at TMT (3.5 and 6.2%). Thus, in this case
162 SPMs accurately represented signal intensity differences. Furthermore, signal intensity increased
163 in all four regions expected to respond to TMT (+2.1-3.9%, $d = 0.85$-1.20, $p < 0.05$ FDR),
164 demonstrating robust TMT-induced enhancement.
165
166 Statistical mapping of ELA mice at HC (Fig. 2) indicated signal enhancements within regions we
167 previously identified to respond to TMT in Std mice (32). To determine the degree of signal intensity
168 differences between ELA and Std at HC and test whether ELA signal truly exceeded Std in these
169 regions, we measured and compared signal intensities within 3 x 3 x 3 voxel ROIs (**Fig. 3B**, ***SI***
170 ***Appendix* Tables S2** and **S4**). Magnitudes of signal enhancement at HC over pre-Mn(II)
171 corresponded to the presence or absence of significant SPM signal for both Std and ELA (non-
172 enhanced: SI = 2.0-3.6%, $d = 0.5$-0.7; enhanced: SI = 6.1-17.9%, $d = 0.96$-5.17). Direct
173 comparisons between groups revealed that ELA intensities were heightened at HC in all four
174 measured regions (SI = 4.1-6.6%, $d > 1.00$, $p < 0.05$ FDR). Thus, ELA signal intensities within
175 threat-responsive regions exceeded that of Std even before threat. ELA also displayed a lower
176 variance than Std.
177

178 Together these observations support the conclusion that differences in SPM-identified activation
179 volumes, at $p < 0.01$ and cluster size ≥ 8 voxels, reliably represent intensity differences between
180 post-Mn(II) images. However, when SPM analysis reveals overlapping anatomy of activation
181 volumes between groups or conditions, direct measurements of post-Mn(II) intensities may be
182 necessary to uncover potential differences in activity levels that are not reflected solely by activation
183 volumes.
184
185 **Mn(II)-Enhanced Signal Corresponds to c-fos Expression.** We next sought to test whether
186 different degrees of Mn(II)-enhancement corresponded to differences in neural excitation, as
187 detected by c-fos expression (33, 42, 64, 65) (**Fig. 4**). To test this hypothesis, from a subset of mice
188 from both groups ($n_{Std} = 5$ and $n_{ELA} = 6$), we selected pairs of regions with varying numbers of c-
189 fos+ nuclei, where anatomy was also identifiable in MR slices: hypothalamus (HYP) and thalamus
190 (THA); superior central raphe (CS) and midbrain (MB) (**Fig. 4A-B**). In both groups, regions with
191 statistically greater numbers of c-fos+ nuclei (HYP vs THA; CS vs MB) also displayed statistically
192 greater Mn(II)-enhanced signal intensities (**Fig. 4C-D**, $p < 0.001$). Robust effect sizes were
193 observed for both modalities (c-fos: d = 3.75-5.03; MEMRI: d = 1.88-6.37). Statistical differences
194 in MR signal intensities from these subsets of mice were replicated in a second subset from each
195 group, demonstrating test-retest reliability (d = 2.94-8.43, $p < 0.001$, FDR) (***SI Appendix* Fig. S4**).
196 To further test whether intensities correlated linearly with c-fos counts, we correlated MEMRI and
197 c-fos data across the four regions with bootstrap resampling and permutation testing. In both
198 groups, we found strong correlations (Std: $r = 0.636$, $p < 0.0001$; ELA: $r = 0.582$, $p < 0.0013$) (**Fig.
199 4E** and ***SI Appendix* Fig. S5**). Thus, our data suggest that the degree of MEMRI signal intensities
200 reflects differences in neural excitation, and further that MEMRI data reflect cumulative activity
201 within a given volume, i.e., density of active neurons as well as the level of activity of those neurons.
202
203 **Deeper Dives into Brain States of Adult Mice Exposed to ELA.** To assign neural activity in ELA
204 mice to specific anatomical regions, we aligned statistical maps of enhanced voxels with our *InVivo*
205 Atlas (***SI Appendix* Table S5**). Then we quantified activity in those anatomically defined segments
206 at each condition with a new approach, fractional activation volumes (FAV) (32) (**Fig. 5**). The FAV
207 is the fraction of activated to total voxels in each segment. Activated voxels were those found to be
208 statistically enhanced in SPM comparisons of post-Mn(II) to pre-Mn(II) images at each condition.
209 FAVs were visualized as column graphs. Comparing column graphs between conditions
210 demonstrated successive changes in FAVs as mice progressed through successive conditions.
211
212 Overlays of statistical maps show that much of the activity at HC coincides with that of TMT in ELA
213 mice ($p < 0.01$ cluster corr., d = 0.79-8.19) (**Fig. 5A** and ***SI Appendix* Table. S6A)**. Some regions

214 expand while a few others contract from HC to TMT. By FAV analysis of ELA, we see that at HC
215 large FAVs were prominent in various domains (OLF, STR/PAL, HYP, and CB) with segments
216 (MOB, MS, BST, and AHN) almost totally active. Immediately after TMT, FAV values were retained
217 or increased, with the largest increases in CEA and LC. Several STR/PAL and THA segments
218 decreased in FAV after TMT, including LSc, LGd and MH. No relationships between segment
219 volume and FAV were observed. Differences in signal intensities between conditions in these
220 segments were also statistically significant by SPM comparisons between successive post-Mn(II)
221 images, with the greatest differences in the LC (***SI Appendix* Fig. S6** and **Table S6B**).
222
223 We then compared segmental FAVs between TMT and D9 of ELA mice to learn how TMT affected
224 brain-wide activity long term (**Fig. 5B**). Segmentation analysis revealed that FAV decreased in
225 three domains (OLF, HB, and CB) with the most substantial change in CB. Most other segments
226 either retained or further increased FAV, particularly within AMY, THA, HYP and MB domains. In
227 many segments where FAV had increased following TMT, FAV at D9 either persisted (LC) or
228 increased (CEA), suggesting a longer lasting effect of the threat experience. Segments where FAV
229 decreased acutely after TMT typically remained low (LSc). Others increased at D9 (MH). These
230 results suggest that brain activity in some segments does not return to pre-threat levels.
231
232 To test whether activities do not return to pre-threat levels, we compared HC with D9 using a similar
233 strategy in both ELA and Std mice (**Fig. 5C and 5D**, also ***SI Appendix* Table S6A**). Both overlays
234 of SPMs and columns graphs of FAV show that at D9 after threat, activity in both ELA and Std was
235 increased substantially compared to HC in many domains (AMY, STR/PAL, HYP, and MB). The
236 magnitude of FAV increase in these domains was twice as large on average in Std than in ELA
237 (+0.28 vs +0.11). This pattern also appeared in pairwise comparisons of post-Mn(II) intensities
238 between conditions (***SI Appendix* Fig. S7** and **Table S6B**). Neither the brain-wide activity of ELA
239 nor Std returned to pre-threat levels at D9. These data suggest regions in the brain remain
240 hyperactive one week or more after acute threat.
241
242 Visualization of brain states at HC and D9 revealed qualitative differences between groups. At HC,
243 before threat, FAVs of ELA were substantially greater than those of Std across many brain
244 segments. These larger FAVs in ELA could not be attributed to procedural differences, such as
245 $MnCl_2$ dosing, MR parameters, imaging timing, image processing, segmentation analysis (***SI***
246 ***Appendix* Fig. S2** and **Table S1**), differences in pre-Mn(II) signal intensities between groups (***SI***
247 ***Appendix* Fig. S8**) or differences in anatomy between groups (***SI Appendix* Fig. S9**). While Std
248 exhibited larger FAV increases from HC to D9 than ELA in most segments, ELA exhibited larger
249 increases than Std in a subset of segments, including RE and LC. In other segments, ELA displayed

250 the opposite directional change from HC to D9 compared to Std, including PA, LSr, IPN, and PCG.
251 Except for IPN, these segments also responded acutely to TMT in ELA (**Fig. 5B**). These findings
252 suggest that brain-wide activity and its evolution from threat-naïve (HC) to threat-experienced (D9)
253 conditions differs between groups and that ELA mice resemble a post-threat-like state already at
254 HC. Furthermore, those segments that respond to TMT in ELA appear to be major contributors to
255 differences between groups at D9. These qualitative observations prompted a direct between-
256 group statistical analysis.
257
258 **ELA Affected Many Segments Within Each Anatomical Domain.** To determine whether signal
259 intensities between ELA and Std differed statistically between groups, and to map the anatomical
260 distribution of those differences, we performed a direct SPM comparison. First, we performed an
261 unpaired t-test comparing baseline pre-Mn(II) images between groups, which revealed small
262 intensity differences (***SI Appendix* Fig. S7**). For subsequent comparisons, post-Mn(II) images were
263 adjusted to correct for these baseline differences. We then compared ELA and Std post-Mn(II)
264 images at each condition by an unpaired SPM t-test ($p < 0.05$, cluster corr., $d = 0.70$-5.30) (**Fig. 6**
265 and **Movie S1**). Segmentations of SPM difference maps were used to calculate the proportion of
266 statistically enhanced voxels (either ELA > Std or Std > ELA) per total voxels in each segmented
267 region at each condition, the fractional difference volume (FDV) (**Fig. 6A-D**, and ***SI Appendix***
268 **Table S7**). At all three conditions, ELA exhibited greater signal intensities than Std (i.e., heightened
269 activity) in most segments but to a lesser extent at D9, supporting observations from the within-
270 group SPMs shown in **Fig. 5**. From HC to D9, the total volume of enhanced voxels in ELA relative
271 to Std decreased by 27%.
272
273 Closer examination of FDVs within different anatomical domains identified heightened activity at
274 HC in ELA compared to Std within OLF, STR/PAL, and HYP domains (**Fig. 6A**, yellow columns).
275 At TMT, differences in these domains decreased, although heightened HYP activity in ELA was
276 somewhat preserved and new differences became noticeable in the CB (**Fig. 6B**). At D9,
277 heightened activity in the HYP domain of ELA returned or even increased (**Fig. 6C**). While
278 heightened activity was present in most HYP segments for each condition, many other domains in
279 ELA exhibited smaller volumes of heightened activity over Std at TMT and D9, particularly
280 segments within STR/PAL. In contrast, ELA exhibited diminished activity compared to Std within
281 only a few segments of CTX, THA, HYP, MB and CB domains (**Fig. 6A-C**, blue columns). Thus,
282 ELA in general displayed heightened brain-wide activity over Std at HC. The number and degree
283 of differences lessened upon experiencing threat in most segments but not in all. Next, we will take
284 a deeper dive into segmental activity dynamics.
285

286 Examining segment-wise FDV across conditions revealed at least five patterns of segmental
287 dynamics (**Fig. 6D**). To facilitate interpretation of activity differences across conditions, we plotted
288 FDVs indicated by arrows in **Fig. 6A-C** as line graphs (**Fig. 6D**). These graphs represent the
289 dynamic patterns of heightened activity in either ELA (yellow) or Std (blue). The *first* pattern across
290 many segments was heightened activity in ELA at HC, which became more similar between groups
291 at TMT (**Fig. 6D**, blue). Some of these segments continued to be similar between groups at D9
292 (e.g., MS) while others returned to heightened activity in ELA (e.g., VMH). A *second* pattern
293 followed an opposite dynamic in response to TMT. In these segments, volumes of heightened ELA
294 activity expanded acutely with TMT and returned to HC levels at D9 (CEA and CS, red). A *third*
295 pattern appeared in a few segments, where FDVs of ELA rose only at D9 (PA and DMH, green). A
296 *fourth* pattern emerged in two segments (DP and ARH, black). Similar to pattern one, ELA activities
297 in these two segments were greater than those of Std at HC and/or D9. Dissimilar to pattern one,
298 ELA activities decreased in these segments below those of Std at TMT. A comparison between
299 male and female found that ELA females might contribute to between-group differences at D9 in
300 VMH, ARH and PA more than ELA males, with sex-differences in PA also present in pre-Mn(II)
301 images (***SI Appendix* Fig. S10**). A single segment followed a *fifth* pattern (LC, purple), where
302 activity was greater in Std at HC and then reversed after TMT through D9 to become heightened
303 in ELA. Together these data demonstrate that brain-wide activity of ELA mice is reconfigured
304 across conditions and that dynamics in response to threat, both brain-wide and segment-wise,
305 differ dramatically from Std.
306
307 **Discussion**
308
309 In this study we mapped the spatial-temporal transformations that ELA imposes on brain-wide
310 activity, as detected initially when in a home cage (HC) environment and then short and long-term
311 after challenge by an acute threat as compared to a Standard, phenotypically "normal," mouse.
312 Three different brain states (66), as defined here by widely distributed patterns of fractional
313 activation volumes among segments, emerged within each group. In all three conditions, brain
314 states of adult mice reared with the fragmented maternal care model for ELA differed from brain
315 states of adult Std mice, with greater overall neural activity after ELA (**Fig. 6E** and ***SI Appendix***
316 **Fig. S11**). Even without provocation, ELA mice at HC had heightened fractional activation volumes
317 in regions known to be activated by predator odor or altered in reward processing: olfactory and
318 hypothalamic segments (65, 67-72), as well as striatum-pallidum (32, 73, 74). Distribution of
319 heightened activity expanded immediately after threat to engage subcortical structures as well as
320 monoaminergic nuclei and deeper brainstem segments in ELA, as also occurred in Std (32). Neither
321 group regained HC activity patterns nine days after threat. Across all conditions, activity in

322 hypothalamus of ELA was higher than Std. At D9, new differences emerged in the ventral
323 hippocampus and posterior amygdala, where activity was greater in ELA. Our longitudinal brain-
324 wide imaging strategy coupled with our computational processing and analytics empowered us to
325 follow these brain states in the same individuals as they progress through this series of experiences
326 in sample sizes sufficient for statistical significance. Our processing pipeline, aligning 192 whole-
327 brain images captured with 100μm^3 resolution, allows precise localization of statistically significant
328 activity common across multiple individuals. This unique capability is not possible with most other
329 physiological approaches.
330
331 We found dynamic changes in segment-wise fractional activation volumes between conditions
332 throughout the brain in both cohorts. When a segment transitions from lower to higher FAV/FDV,
333 we predict that segment to have a more dominant functional role within its connectome. For
334 example in ELA, the increased volume of activity In CEA (from 43% to 53%) as the mouse
335 progresses from home cage to immediately after threat may contribute to heightened activity
336 throughout threat circuity (75). That ELA mice sustained heightened CEA activity at all three
337 conditions, suggests that ELA leads to persistent engagement of threat circuitry. This sustained
338 engagement of threat circuitry after ELA may sensitize CS and LC to threat, promoting
339 monoaminergic modulation of segmental activities toward the patterns observed at D9 (76-79).
340 Differing levels of activity among segments of a single network across different conditions could
341 produce different internal states (80, 81) and/or outcomes from that same network, be they actions,
342 decisions, emotions, thoughts, memories, or creative works, such as music, poetry, or art.
343
344 Results presented here should be considered in light of several limitations. 1) Theoretically, small
345 variations in rearing environment could contribute to differences between groups not attributable to
346 ELA. However, multi-site studies in mice find that different breeding/rearing facilities have no effect
347 on stress reactivity (82) and minimal explanatory value for at least 14 other physiological measures
348 (83). JAX-reared mice are the phenotypical standard and the most commonly used mouse by
349 researchers globally (9), making them an invaluable comparison group to generalize findings
350 across research facilities (84). 2) Although we found minimal sex differences between male and
351 female ELA mice, we cannot fully attribute heightened activity in HYP and vHIP/AMY segments to
352 ELA because we only had a small sample size and because our Std group was all male. Other
353 studies suggest a combinatorial effect of ELA and sex is likely within these threat responsive
354 regions (71, 85, 86). 3) To what degree does Mn(II) signal faithfully represent neural activity?
355 Staining by c-fos shown here and previous reports (32, 36-39, 42, 87, 88) contend that Mn(II) tags
356 active neurons, though minor non-calcium-dependent mechanisms may exist (88, 89). The amount
357 that accumulates and the rate of Mn(II) transport within axons cannot explain changes in segmental

358 signal intensities between HC and TMT, nor the new pattern of segmental activity at D9. 4)
359 Spatiotemporal resolution of MEMRI is less granular than some other methods. At 100 μm^3 voxels,
360 our MEMRI is better than current BOLD imaging but still not at the level of single neurons studied
361 with electrophysiology. MEMRI temporal resolution is less than either BOLD imaging or
362 electrophysiology. However, MEMRI's capacity for repeated longitudinal brain-wide imaging across
363 a long time span of neural activity in awake, freely moving mice makes these tradeoffs worthwhile.
364 MEMRI pinpoints regions worthy of study at greater resolutions by other techniques. 5) Small
365 anatomical variations could have influenced our results (90-93). However, our Jacobian
366 deformation analysis reported minimal alterations in anatomical volumes, and our SPM analysis
367 accounted for any signal differences by preserving intensity concentrations within voxels (94, 95).
368 6) We recognize that statistical methods are limited due to the choice of thresholding and pre-
369 preprocessing, which is particularly difficult with MRI (33, 96-98). We minimized these potential
370 issues by rigorously examining each processing step for image quality, by ensuring sample size
371 was sufficient to detect moderate to large signal enhancements from Mn(II), and by selecting
372 statistical thresholds based on effect size and false positive rate corrections. 7) Atlas segmentation
373 yields volumes that vary widely, 10^1-10^4 voxels. This may lead us to miss some large segments
374 where small- to medium-sized activations only produce small fractional volumes.
375
376 In conclusion, ELA has a brain-wide impact on balance of neural activity among widely distributed
377 sub-regions and their dynamics across a series of experiences, from freely moving exploration in
378 the home cage to immediate- and post-threat conditions. We identify specific subcomponents of
379 this brain-wide network that are differentially activated depending upon condition in adult mice who
380 experienced ELA and compare these with the standard, commonly studied, adult mouse. Future
381 studies dissecting the functional connections suggested by these MEMRI results will provide
382 valuable information on coordination of coactivated regions. A next step will be to determine the
383 functional significance of these disparate segmental activities, how they interact in a serially
384 dependent manner to reconfigure future brain states, and whether these interactions contribute to
385 vulnerabilities for mental health disorders and/or compulsive drug use. Ultimately this longitudinal
386 MEMRI technique will provide insights into neurophysiological/biochemical mechanisms
387 contributing to the reconfiguration of brain states by ELA and inspire reparative/restorative
388 interventions to protect from the harm of ELA and secondary traumatic events later in adulthood.
389
390 **Materials and Methods**
391
392 **Mice.** Animal protocols were approved by Institutional Animal Care and Use Committees at both
393 California Institute of Technology (Caltech) and University of New Mexico. Numbers were

394 determined by statistical power analyses. Both Std and ELA reared groups of C57BL/6J mice
395 (Stock No: 000664) were bred at Jackson Labs (JAX). Adults from each group went through parallel
396 acute threat timelines, were handled by the same experimentalists, and imaged at Caltech (n = 24,
397 12 in each group), in a series of experiments performed over a period of 3.8 years. For ELA, we
398 followed a fragmented care protocol (11, 12). Longitudinal MEMRI commenced at ages 11-13 wk.
399 This age was chosen because brain development is considered largely complete by 3 months (99).
400 Equal numbers of male (n = 6) and female (n = 6) ELA pups were used from 5 weaning groups.
401 Twelve male Std mice selected from 5 different weaning cages were subjected to the longitudinal
402 experimental protocol. No litter/cage effects were detected for either group.
403
404 **Video Recordings and Acute Threat Exposure**. We followed our previously published
405 longitudinal imaging protocol (32). Briefly, prior to imaging and during TMT exposure mice were
406 tracked in a custom arena using Noldus Ethovision (XT15) (32, 100, 101). Prior to TMT exposure,
407 mice were bright, alert and responsive, and displayed normal motility. Percentage of time spent in
408 light side of the arena and distance travelled in the arena were calculated and statistically evaluated
409 with FDR correction in R v4.2.1 (*nlme* and *emmeans* packages) (102-107). Graphs were generated
410 in R (*ggplot2*) (108).
411
412 **Longitudinal MEMRI.** After capture of a non-enhanced image, mice were injected i.p. with 0.3
413 mmol/kg of $MnCl_2$-$4H_20$ in sterile buffered saline and then imaged with contrast according to the
414 timeline previously reported (32). Between scanning sessions, video recordings, or $MnCl_2$
415 injections, mice were returned to their home cage. Mn(II) kinetics were followed by ROI analysis
416 across the timeline to test for expected intensity patterns. For optimization of MEMRI imaging
417 parameters, refer to our review (33).
418
419 **MR Image Pre-Processing.** MR images from both groups were pre-processed together in batch
420 according to standardized protocols (33, 49, 51). Briefly, raw MR image quality was visually
421 assessed and SNR quantified. Image artifacts were corrected when needed and outlier images
422 excluded from statistical analyses. Std and ELA pre- and post-Mn(II) images were then skull-
423 stripped, intensity normalized and anatomically aligned together in batch. Each processing step
424 was verified and validated (***SI Appendix* Fig. S1-2**).
425
426 **MR Image Analysis.** *Comparison of Anatomy Between Groups.* For comparison of anatomy
427 between groups, we calculated Jacobian Determinants of the Deformation fields generated by the
428 affine-nonlinear alignment step. Average Jacobian determinant values were calculated using our

429 atlas-based segmentation process (see below). Two sample t-tests between Std and ELA values
430 were performed for each segment, FDR correction.
431
432 *Measurement and Analysis of MR Intensities in ROIs.* Measurements were made from pre- and
433 post-Mn(II)-enhanced MR images that had been skull-stripped, scaled, and aligned. Coordinates
434 (x/y/z) for regions of interest (3 x 3 x 3 voxels) were selected by projecting the annotated atlas
435 labels onto the aligned grayscale template in FSLeyes and placing the crosshairs within segments
436 that appeared different in SPM comparisons to pre-Mn(II) and that corresponded to previously
437 reported TMT-responsive regions (32, 75). Mean intensities from ROI measurements were
438 compared by paired and two-sample t-tests in R (*t.test)*, and effect sizes and FDR adjustments
439 were calculated (*effectsize* and *p.adjust)*.
440
441 *Statistical Parametric Mapping (SPM).* For SPM, all images were smoothed to meet SPM
442 assumptions with a 0.15 mm^3 Gaussian kernel, the minimum size allowable (56, 95). We adjusted
443 for small baseline differences between groups in their pre-Mn(II) images by subtracting the average
444 voxel-wise differences of intensities from each of the ELA images. After this adjustment, an
445 unpaired t-test of pre-Mn(II) images yielded no voxels with significant differences between groups.
446 Voxel-wise T-maps of statistically significant differences between images of different conditions
447 within group (paired t-test) or between groups (unpaired t-test) were calculated using SPM12 (95).
448 Statistical maps were cluster corrected (*cluster corr.*) in SPM12 with a minimum cluster size of 8
449 voxels (95). Fiber tracts and ventricles segments were masked from statistical maps using our
450 *InVivo* Atlas. Setting statistical thresholds included consideration of minimal detectable effects and
451 smallest cluster size needed to remove false positives while minimizing loss of signal.
452
453 *Atlas Alignment, Segmentation, and Calculation of Fractional Volumes.* Our updated *InVivo* Atlas
454 grayscale image was inversely aligned to the dataset, and the warp field applied to the label image.
455 This permitted automated segmentation of the images into 117 regions (32). Segment masks were
456 created and applied using *fslmaths*. The number of statistically enhanced voxels were identified as
457 those from SPM paired or unpaired t-tests exceeding thresholds set according to our criteria
458 described above. The number of total voxels within each segment were counted using *fslstats* (24).
459 The fraction of enhanced voxels from SPM paired (FAV) or unpaired (FDV) t-tests to total voxels
460 within each segment were calculated in R and visualized as column graphs and line plots using
461 *ggplot2* (107-109).
462
463 **Immunohistochemistry, c-fos Quantification and Correlation to MEMRI.** Brains were prepared
464 for histology after D9 according to our protocol (5 Std and 6 ELA) (32, 110). We selected 1-3

465 sections also identifiable in MR slices that had regions with both very high and very low numbers
466 of c-fos stained nuclei. Nuclei were counted in a 3 x 3 grid of 100 μm^2 squares from 1-3 x 35 µm
467 thick sections of each brain, and MR intensities (SI) measured from 100 μm^3 voxels in
468 corresponding slices. Counts and SI were visualized in quartile boxplots with R (*ggplot2*). A square
469 root transformation linearized c-fos+ count data for determination of effect size and statistical
470 significance. Regions counted in the same section or measured in the same slice were compared
471 by linear mixed models and by post-hoc paired t-tests with FDR correction. Counts and SI of each
472 group were averaged by region and individual and then correlated, with p-value determined by
473 permutation testing.
474
475 Please see ***SI Appendix*** **Extended Methods** for additional methodological details.
476
477 **Acknowledgments**
478 We gratefully acknowledge the Beckman Institute at Caltech and many support staff, faculty and
479 trainees (see ***SI Appendix***). Supported by NIH R01MH096093 (ELB), NIH NIA P20AG068077
480 (ELB), NIH NINDS F99NS139535 (TWU), Zilkha Neurogenetic Institute (REJ) and Harvey Family
481 Endowment (ELB).

Figures and Tables

Figure 1.

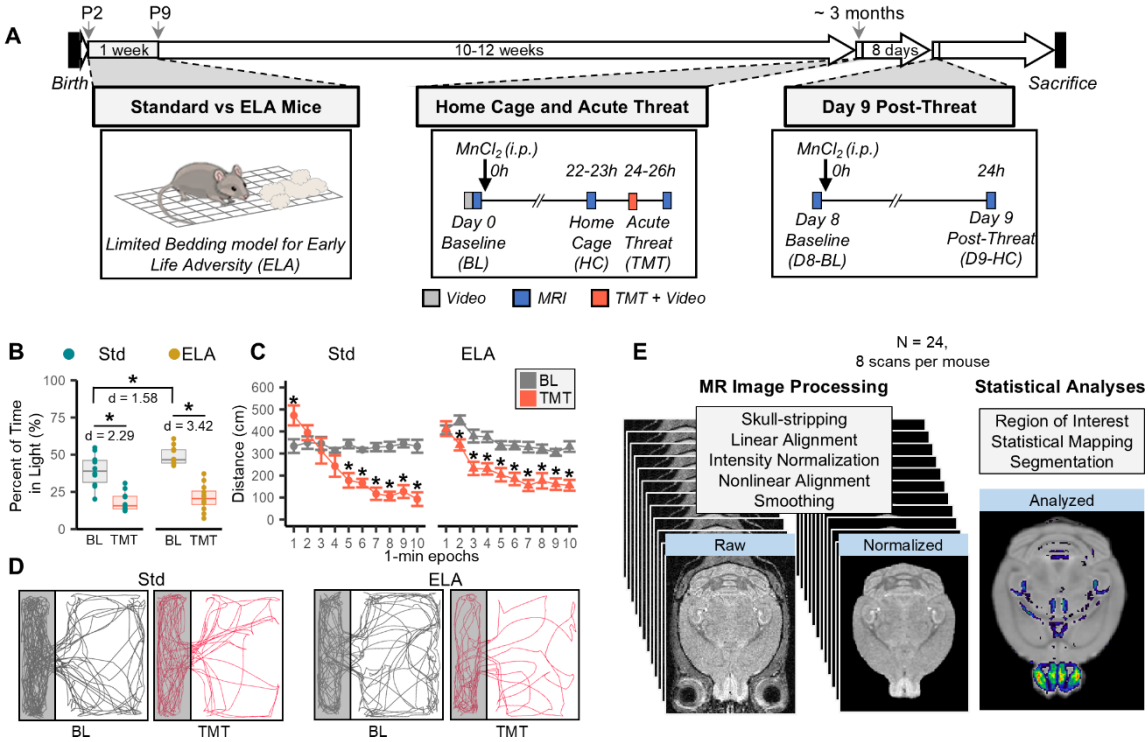

Fig. 1. Longitudinal imaging procedures. *(A)* Schematic of the overall timeline (open arrows, top). Boxes diagram events. *Left box*: ELA paradigm; *Middle box*: Home Cage and Acute Threat, timeline of MR and video capture: Baseline, BL; Home Cage, HC; Acute Threat, TMT. *Right box*: Day 8 Baseline, D8-BL; Day 9 Post-Threat, D9-H. *(B-D)* Video tracking results: *(B)* Percent time spent in the light (quartile boxplots, individuals indicated by dot plot overlays) (cyan, Std; yellow, ELA; BL and TMT as per schematic). *(C)* Distance traveled after imaging during TMT exposure. Line graphs of distance travelled per 1-min epochs with error bars representing standard error of the mean. Repeated measures ANOVA with fixed effects of group and condition. For (B-C), paired and unpaired t-tests with FDR correction for multiple comparisons; Cohen's D effect sizes (d); * $p < 0.05$, n = 22 (10 Std, 12 ELA). *(D)* Representative tracking of one mouse from each group, Std and ELA, at BL (gray) and TMT (red). Shaded areas represent dark side of the arena. *(E)* Overview of MR data processing and analysis used in this study (also see ***SI Appendix* Fig. S1-2**) (33, 49, 51).

498 **Figure 2.**

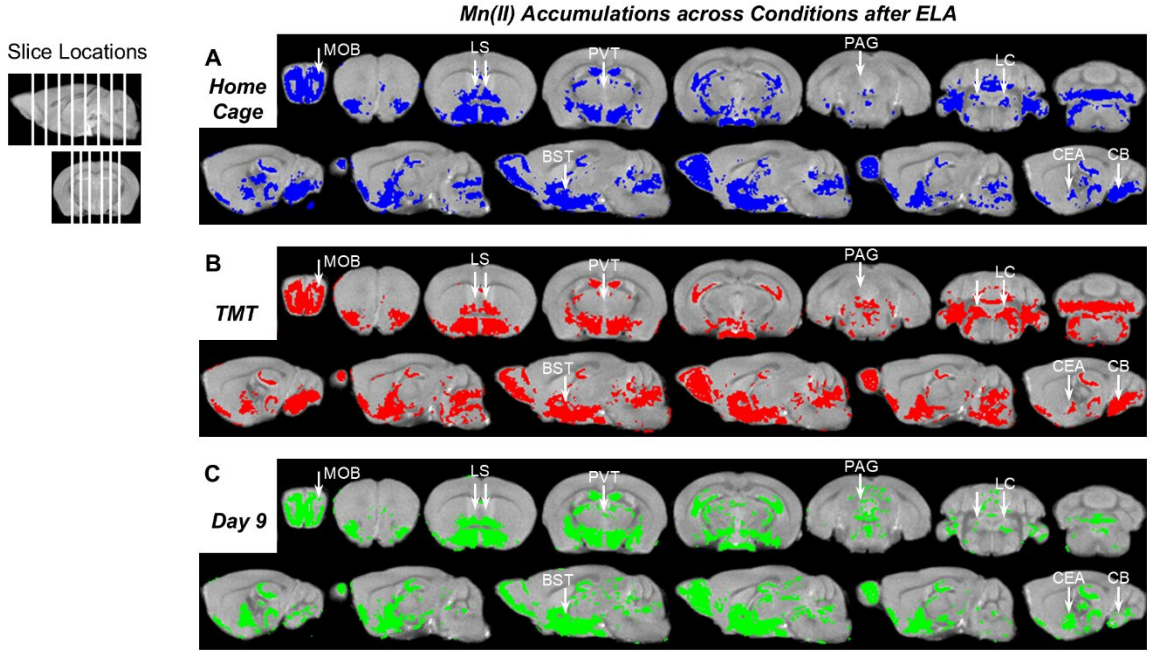

499

500 **Fig. 2.** Statistical parametric maps of MEMRI in ELA mice change as they progress from home
501 cage to acute threat to post threat. *(A-C)* Shown are statistical maps of voxel-wise paired t-tests of
502 post-Mn(II) images of ELA mice at each successive condition compared to their pre-Mn(II) images.
503 Maps are overlaid on the grayscale dataset average of all pre-Mn(II) images (coronal slices, top
504 rows; sagittal, bottom rows). Slice position is indicated on the grayscale image (top left, white lines).
505 White arrows indicate notable differences between conditions. MOB, main olfactory bulb; LS, lateral
506 septum; BST, bed nuclei of the stria terminalis; PVT, paraventricular thalamus; HIP, hippocampus;
507 LC, locus coeruleus; CEA, central amygdala; and CB, cerebellum. For t-tests, $n = 12$, $p < 0.01$, T
508 $= 2.72$, cluster corr. For comparisons between conditions of ELA mice see ***SI Appendix***, **Fig. S3**.
509

510 **Figure 3.**

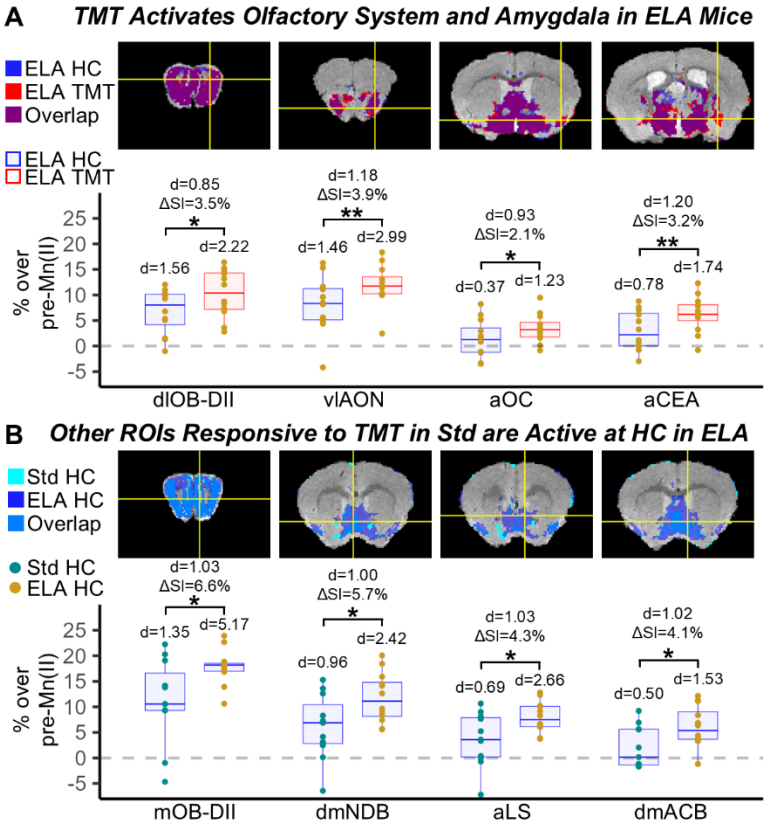

511

512 **Fig. 3.** Measurements of MEMRI signal intensities in candidate regions of interest in systems
513 known to be involved in predator odor-type threat responses. *(A) Top*: Representative slices from
514 two voxel-wise statistical maps (ELA HC & ELA TMT) of post-Mn(II) > pre-Mn(II) superimposed
515 onto the grayscale *InVivo* atlas. SPM paired t-tests: $p < 0.01$ cluster corr. ROI locations selected
516 where TMT signal did not overlap with HC (yellow crosshairs). *Bottom*: Quartile boxplots of signal
517 intensity as a percent over pre-Mn(II) measured in each ROI. Effect sizes of the differences in signal
518 between conditions at each ROI (Cohen's D, d) and average signal intensity differences (ΔSI)
519 between the two conditions are indicated. Paired t-test, * $p < 0.05$, ** $p < 0.01$, FDR. dIOB-DII,
520 dorsal lateral DII olfactory subdomain; vlAON, ventrolateral anterior olfactory nucleus; aOC,
521 anterior olfactory cortex; and aCEA, anterior central amygdala. *(B) Top*: Similar comparison but
522 between groups at one condition, HC. Slices of paired t-tests of HC greater than pre-Mn(II) from
523 either Std or ELA are superimposed on the grayscale atlas. Crosshairs indicate ROI locations,
524 selected where ELA signal did not overlap with Std. *Bottom*: Quartile boxplots of unpaired t-tests
525 of ROI measurements: * $p < 0.05$, FDR. mOB-DII, medial DII olfactory subdomain; dmNDB,
526 dorsomedial diagonal band nucleus; aLS, anterior lateral septum; dmACB, dorsomedial nucleus
527 accumbens. See ROI coordinates and summary statistics in ***SI Appendix,* Tables S2-4**.

528

Figure 4.

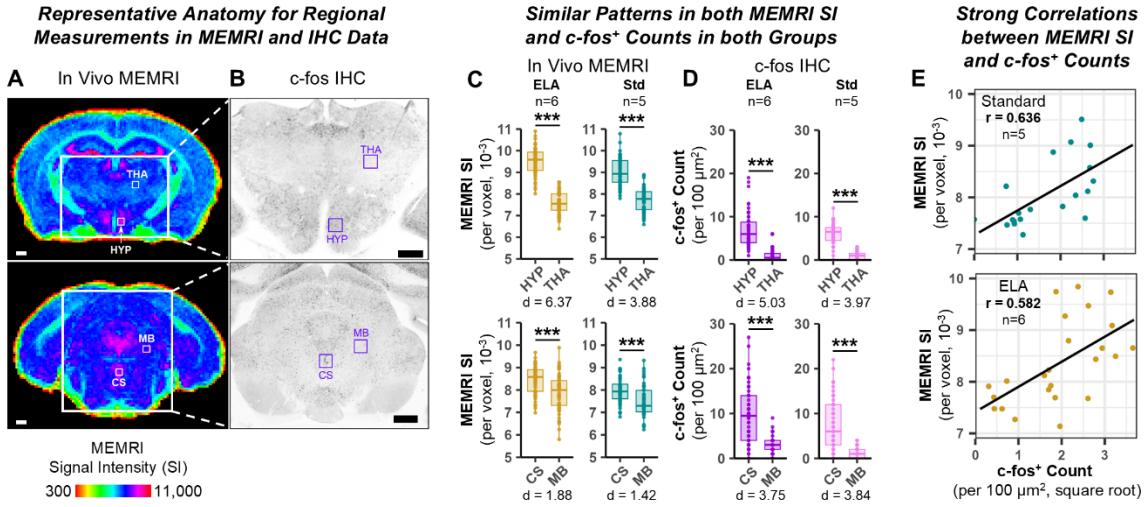

Fig. 4. MEMRI and c-fos staining correlate. (*A*) Coronal slices of the average intensities of day-9 post-Mn(II) images (color code, bottom) (n = 6). Minimum (300 a.u.) based average noise and maximum (11,000 a.u.) from intensity histograms. Small white boxes indicate regions (3 x 3 x 1 voxels) where signal intensities (SI) were measured. HYP, hypothalamus; THA, thalamus; CS, superior central raphe; MB, midbrain. Mag bar = 500 μm. (*B*) Two representative histological sections from one of the mice contributing to *(A)* stained for c-fos corresponding to anatomy of slices in *(A)* (large white boxes). Purple boxes indicate locations of 3 x 3 grid of 100 μm^2 squares where numbers of c-fos+ nuclei were counted. Mag bar = 500 μm. See ***SI Appendix* Fig. S5A-B** for corresponding images from Std. *(C)* Statistical comparisons of MEMRI SI in four locations for both groups. Shown are quartile boxplots with dot plot overlays of MEMRI SI from ELA (yellow, left) and Std (cyan, right). Paired t-tests were performed between regions within the same slice. Note large Cohen's D effect sizes (d) for paired t-tests between active and inactive regions. For evidence of test-retest reliability of MEMRI SI, see ***SI Appendix* Fig. S4**. *(D)* c-fos counts paralleled MEMRI SI with high or low numbers of c-fos+ nuclei. Shown are quartile boxplots with dot plot overlay of raw c-fos+ counts from ELA (purple, left) and Std (pink, right). A square root transformation linearized c-fos+ counts for statistics. Note similar large Cohen's D effect sizes (d) between active and inactive regions. *(E)* Strong Pearson correlations between MEMRI SI and numbers of c-fos+ nuclei (linearized) when paired by individual. Scatter plots with linear regressions (black lines) of MEMRI SI (vertical axes) by c-fos+ counts (horizontal axes). Points represent the average values for each of the 4 regions across 5 Std (*top*, *cyan*) and 6 ELA (*bottom*, *yellow*) brains. Note strong correlations in both groups (r_{Std} = 0.636, r_{ELA} = 0.582). For paired t-tests in *(C-D)*, *** $p < 0.001$, FDR corrected. For *(E)*, $p < 0.001$ by permutation testing and bootstrapping. Also see ***SI Appendix* Fig. S5C-D**.

Figure 5.

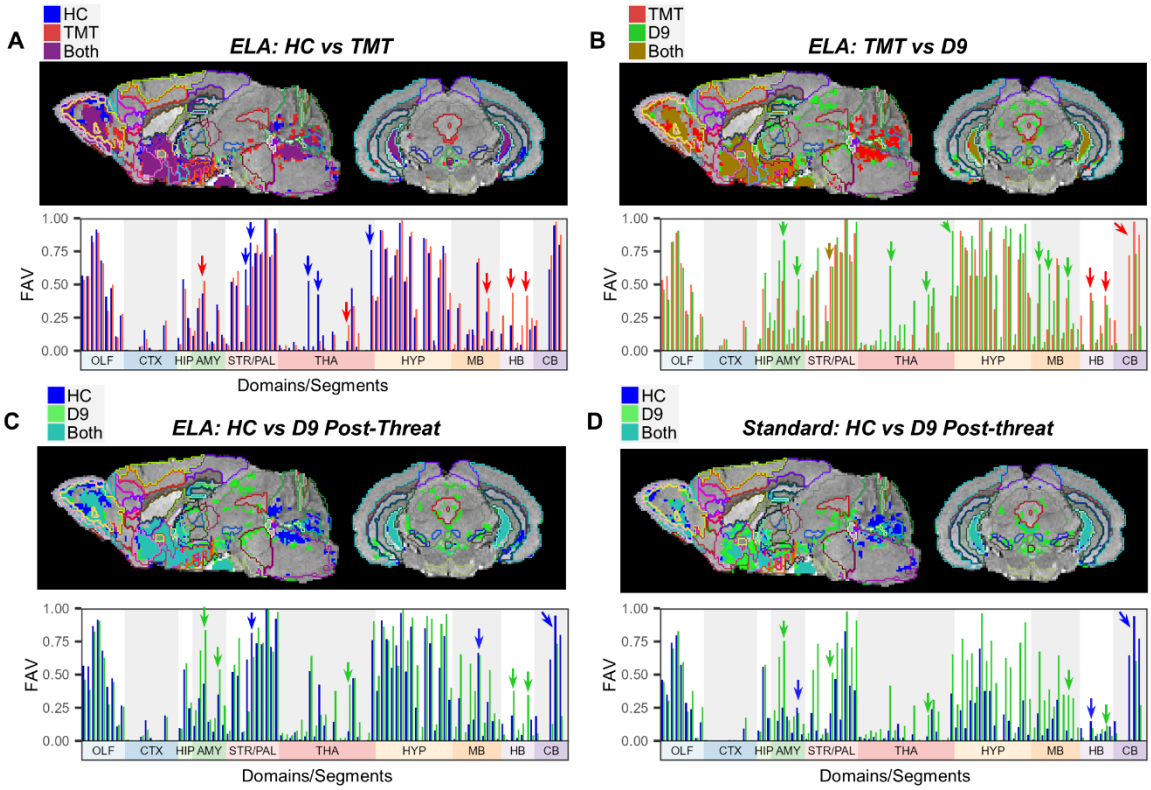

Fig. 5. Statistical maps show progressive modifications of activity across sequential conditions. *(A-D)* Voxel-wise paired t-tests of post-Mn(II) compared to pre-Mn(II) images at two conditions: in ELA mice, *(A)* HC (blue) and TMT (red), *(B)* TMT (red) and D9 (green), and *(C)* HC (blue) and D9 (green); and in Std mice, *(D)* HC (blue) and D9 (green). *Top*: Pairs of statistical maps were projected onto the grayscale *InVivo* Atlas with segments outlined to show the anatomical overlaps between conditions. *Bottom*: Corresponding column graphs show segment-wise fractional activation volumes (FAV, vertical axes) quantified from segmentations of statistical maps. Anatomical domains (color-coded on horizontal axes) are divided into 101 segments. Arrows point to examples of segments with FAV alterations between conditions and color-coded to indicate direction of change. For paired t-tests, $p < 0.01$, cluster *corr.* for multiple comparisons. ELA, $T_{(11)} = 2.72$, $d \geq 0.79$, $n = 12$; Std, $T_{(10)} = 2.76$, $d \geq 0.83$, $n = 11$. See ***SI Appendix*** **Table S5** for list of domains and segments, and **Table S6A-B** for FAV values.

Figure 6.

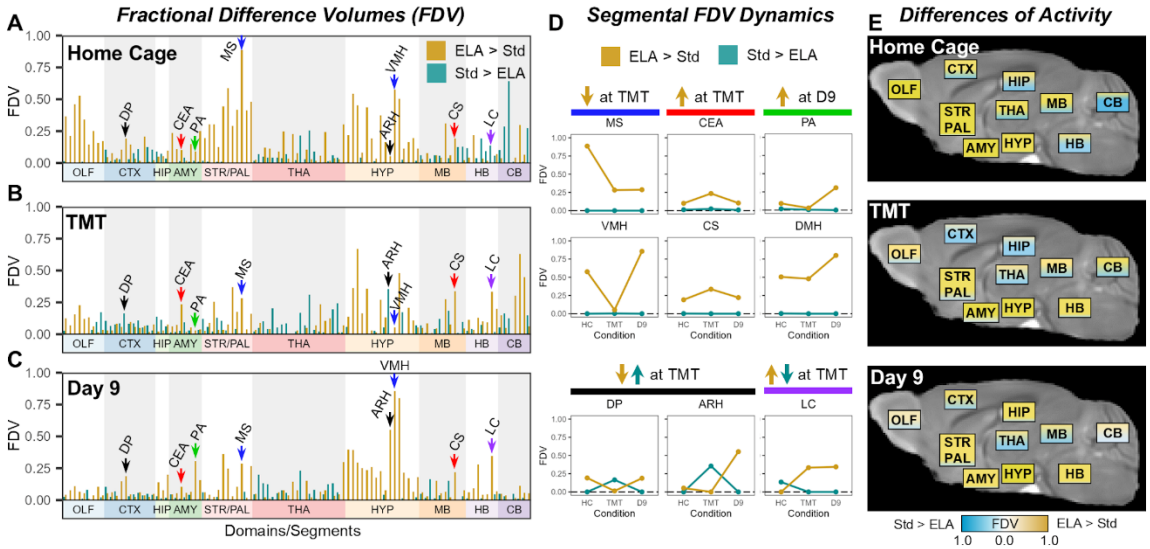

Fig. 6. ELA brain states differ from Std at every condition. *(A-C)* Fractional Difference Volumes (FDVs) from segmentation of unpaired SPM t-tests between signal intensities of ELA and Std at *(A)* HC, *(B)* TMT and *(C)* D9 conditions. All ELA images were adjusted for the voxel-wise average differences between groups' pre-Mn(II) images. FDV color-code represents where ELA signal intensities were heightened (yellow) or diminished (blue) relative to Std. Arrows in column graphs point to example segments with notable FDV dynamics as in *(D)*: blue, MS and VMH; red, CEA and CS; green, PA and DMH; black, DP and ARH; and purple, LC. *(D)* Shown are examples of various dynamics in FDV in 9 segments, which were highlighted by arrows in column graphs *(A-C)*. Line graphs show FDVs (vertical axes) of each segment across three successive conditions (horizontal axes). Graphs are grouped and color-coded according to the dynamical pattern of ELA and Std FDV values. *(A-D)* Unpaired t-tests, $p < 0.05$, cluster corr.; HC: $T_{(21)} = 1.72$, $n_{Std} = 11$, $n_{ELA} = 12$; TMT and D9: $T_{(22)} = 1.72$, n = 12 per group. *(E)* Three schematics summarizing differences in activity between ELA and Std across the 10 segmented anatomical domains at each condition: HC (*top*), TMT (*middle*) and D9 (*bottom*). Each color gradient corresponds to magnitudes and direction of segmental fractional difference volumes (FDV), and proportion of coloring indicating proportion of segments following that pattern within each domain; See **SI Appendix Movie 1** for a slice-by-slice walkthrough of between group SPMs at each condition projected on brain anatomy, **Table S8** for FDV values and **Table S6** for list of domains and segments.

591 **References**

592

593 1. Felitti VJ*, et al.* (1998) Relationship of Childhood Abuse and Household Dysfunction to
594 Many of the Leading Causes of Death in Adults. *American Journal of Preventive*
595 *Medicine* 14(4):245-258.
596 2. Merrick M*, et al.* (2019) Vital Signs: Estimated Proportion of Adult Health Problems
597 Attributable to Adverse Childhood Experiences and Implications for Prevention — 25
598 States, 2015–2017. *MMWR. Morbidity and Mortality Weekly Report* 68.
599 3. Zarse EM*, et al.* (2019) The adverse childhood experiences questionnaire: Two decades
600 of research on childhood trauma as a primary cause of adult mental illness, addiction,
601 and medical diseases. *Cogent Medicine* 6(1):1581447.
602 4. Spadoni AD*, et al.* (2022) Contribution of early-life unpredictability to neuropsychiatric
603 symptom patterns in adulthood. *Depression and Anxiety* 39(10-11):706-717.
604 5. Yehuda R*, et al.* (2010) Putative biological mechanisms for the association between early
605 life adversity and the subsequent development of PTSD. *Psychopharmacology*
606 212(3):405-417.
607 6. Chen Y & Baram TZ (2016) Toward Understanding How Early-Life Stress Reprograms
608 Cognitive and Emotional Brain Networks. *Neuropsychopharmacology* 41(1):197-206.
609 7. Kraaijenvanger EJ*, et al.* (2020) Impact of early life adversities on human brain
610 functioning: A coordinate-based meta-analysis. *Neuroscience & Biobehavioral Reviews*
611 113:62-76.
612 8. Malave L, Van Dijk MT, & Anacker C (2022) Early life adversity shapes neural circuit
613 function during sensitive postnatal developmental periods. *Translational Psychiatry*
614 12(1):306.
615 9. Garcia-Arocena D (2015) More researchers are using B6J mice than ever before. (The
616 Jackson Laboratory).
617 10. Laboratory TJ (2024) Mouse Room Conditions.
618 11. Molet J, Maras PM, Avishai-Eliner S, & Baram TZ (2014) Naturalistic rodent models of
619 chronic early-life stress. *Developmental Psychobiology* 56(8):1675-1688.
620 12. Rice CJ, Sandman CA, Lenjavi MR, & Baram TZ (2008) A Novel Mouse Model for Acute
621 and Long-Lasting Consequences of Early Life Stress. *Endocrinology* 149(10):4892-4900.
622 13. Bercum FM, Navarro Gomez MJ, & Saddoris MP (2021) Elevated fear responses to
623 threatening cues in rats with early life stress is associated with greater excitability and
624 loss of gamma oscillations in ventral-medial prefrontal cortex. *Neurobiol Learn Mem*
625 185:107541.

626 14. Bolton JL*, et al.* (2018) Anhedonia Following Early-Life Adversity Involves Aberrant
627 Interaction of Reward and Anxiety Circuits and Is Reversed by Partial Silencing of
628 Amygdala Corticotropin-Releasing Hormone Gene. *Biological Psychiatry* 83(2):137-147.
629 15. Bolton JL*, et al.* (2022) Early stress-induced impaired microglial pruning of excitatory
630 synapses on immature CRH-expressing neurons provokes aberrant adult stress
631 responses. *Cell Rep* 38(13):110600.
632 16. Brosens N, Simon C, Kessels HW, Lucassen PJ, & Krugers HJ (2023) Early life stress
633 lastingly alters the function and AMPA-receptor composition of glutamatergic synapses in
634 the hippocampus of male mice. *J Neuroendocrinol* 35(12):e13346.
635 17. de Carvalho G, Khoja S, Haile MT, & Chen LY (2023) Early life adversity impaired dorsal
636 striatal synaptic transmission and behavioral adaptability to appropriate action selection
637 in a sex-dependent manner. *Front Synaptic Neurosci* 15:1128640.
638 18. Guadagno A*, et al.* (2018) Reduced resting-state functional connectivity of the basolateral
639 amygdala to the medial prefrontal cortex in preweaning rats exposed to chronic early-life
640 stress. *Brain Struct Funct* 223(8):3711-3729.
641 19. Guadagno A, Verlezza S, Long H, Wong TP, & Walker CD (2020) It Is All in the Right
642 Amygdala: Increased Synaptic Plasticity and Perineuronal Nets in Male, But Not Female,
643 Juvenile Rat Pups after Exposure to Early-Life Stress. *The Journal of neuroscience : the*
644 *official journal of the Society for Neuroscience* 40(43):8276-8291.
645 20. Guadagno A, Wong TP, & Walker CD (2018) Morphological and functional changes in
646 the preweaning basolateral amygdala induced by early chronic stress associate with
647 anxiety and fear behavior in adult male, but not female rats. *Prog Neuropsychopharmacol*
648 *Biol Psychiatry* 81:25-37.
649 21. Gunn BG*, et al.* (2013) Dysfunctional astrocytic and synaptic regulation of hypothalamic
650 glutamatergic transmission in a mouse model of early-life adversity: relevance to
651 neurosteroids and programming of the stress response. *The Journal of neuroscience :*
652 *the official journal of the Society for Neuroscience* 33(50):19534-19554.
653 22. Johnson FK*, et al.* (2018) Amygdala hyper-connectivity in a mouse model of
654 unpredictable early life stress. *Transl Psychiatry* 8(1):49.
655 23. Kooiker CL, Chen Y, Birnie MT, & Baram TZ (2023) Genetic Tagging Uncovers a Robust,
656 Selective Activation of the Thalamic Paraventricular Nucleus by Adverse Experiences
657 Early in Life. *Biol Psychiatry Glob Open Sci* 3(4):746-755.
658 24. Levis SC*, et al.* (2022) Enduring disruption of reward and stress circuit activities by early-
659 life adversity in male rats. *Transl Psychiatry* 12(1):251.

660 25. Malter Cohen M*, et al.* (2013) Early-life stress has persistent effects on amygdala
661 function and development in mice and humans. *Proc Natl Acad Sci U S A* 110(45):18274-
662 18278.
663 26. Raineki C, Cortes MR, Belnoue L, & Sullivan RM (2012) Effects of early-life abuse differ
664 across development: infant social behavior deficits are followed by adolescent
665 depressive-like behaviors mediated by the amygdala. *The Journal of neuroscience : the*
666 *official journal of the Society for Neuroscience* 32(22):7758-7765.
667 27. Yan CG*, et al.* (2017) Aberrant development of intrinsic brain activity in a rat model of
668 caregiver maltreatment of offspring. *Transl Psychiatry* 7(1):e1005.
669 28. Holschneider DP, Guo Y, Mayer EA, & Wang Z (2016) Early life stress elicits visceral
670 hyperalgesia and functional reorganization of pain circuits in adult rats. *Neurobiol Stress*
671 3:8-22.
672 29. Islam R*, et al.* (2024) Early adversity causes sex-specific deficits in perforant pathway
673 connectivity and contextual memory in adolescent mice. *Biol Sex Differ* 15(1):39.
674 30. White JD*, et al.* (2020) Early life stress causes sex-specific changes in adult fronto-limbic
675 connectivity that differentially drive learning. *Elife* 9.
676 31. Kooiker CL*, et al.* (2024) Paraventricular Thalamus Neuronal Ensembles Encode Early-
677 life Adversity and Mediate the Consequent Sex-dependent Disruptions of Adult Reward
678 Behaviors. (Cold Spring Harbor Laboratory).
679 32. Uselman TW, Barto DR, Jacobs RE, & Bearer EL (2020) Evolution of brain-wide activity
680 in the awake behaving mouse after acute fear by longitudinal manganese-enhanced MRI.
681 *Neuroimage* 222:116975.
682 33. Uselman TW, Medina CS, Gray HB, Jacobs RE, & Bearer EL (2022) Longitudinal
683 manganese-enhanced magnetic resonance imaging of neural projections and
684 activity.e4675.
685 34. Vousden DA*, et al.* (2018) Continuous manganese delivery via osmotic pumps for
686 manganese-enhanced mouse MRI does not impair spatial learning but leads to skin
687 ulceration. *NeuroImage* 173:411-420.
688 35. Aoki I, Wu YJ, Silva AC, Lynch RM, & Koretsky AP (2004) In vivo detection of
689 neuroarchitecture in the rodent brain using manganese-enhanced MRI. *Neuroimage*
690 22(3):1046-1059.
691 36. Bedenk BT*, et al.* (2018) Mn(2+) dynamics in manganese-enhanced MRI (MEMRI):
692 Cav1.2 channel-mediated uptake and preferential accumulation in projection terminals.
693 *Neuroimage* 169:374-382.
694 37. Narita K, Kawasaki F, & Kita H (1990) Mn and Mg influxes through Ca channels of motor
695 nerve terminals are prevented by verapamil in frogs. *Brain research* 510(2):289-295.

696 38. Lin YJ & Koretsky AP (1997) Manganese ion enhances T1-weighted MRI during brain
697 activation: an approach to direct imaging of brain function. *Magnetic resonance in*
698 *medicine* 38(3):378-388.
699 39. Svehla P, Bedecarrats A, Jahn C, Nargeot R, & Ciobanu L (2018) Intracellular
700 manganese enhanced MRI signals reflect the frequency of action potentials in Aplysia
701 neurons. *J Neurosci Methods* 295:121-128.
702 40. Yu X, Sanes DH, Aristizabal O, Wadghiri YZ, & Turnbull DH (2007) Large-scale
703 reorganization of the tonotopic map in mouse auditory midbrain revealed by MRI.
704 *Proceedings of the National Academy of Sciences* 104(29):12193-12198.
705 41. Yu X, Wadghiri YZ, Sanes DH, & Turnbull DH (2005) In vivo auditory brain mapping in
706 mice with Mn-enhanced MRI. *Nature Neuroscience* 8(7):961-968.
707 42. Malkova NV, Gallagher JJ, Yu CZ, Jacobs RE, & Patterson PH (2014) Manganese-
708 enhanced magnetic resonance imaging reveals increased DOI-induced brain activity in a
709 mouse model of schizophrenia. *Proc Natl Acad Sci U S A* 111(24):E2492-2500.
710 43. Bearer EL*, et al.* (2007) Role of neuronal activity and kinesin on tract tracing by
711 manganese-enhanced MRI (MEMRI). *Neuroimage* 37 Suppl 1:S37-46.
712 44. Bearer EL, Zhang X, & Jacobs RE (2007) Live imaging of neuronal connections by
713 magnetic resonance: Robust transport in the hippocampal–septal memory circuit in a
714 mouse model of Down syndrome. *NeuroImage* 37(1):230-242.
715 45. Bearer EL, Zhang X, Janvelyan D, Boulat B, & Jacobs RE (2009) Reward circuitry is
716 perturbed in the absence of the serotonin transporter. *Neuroimage* 46(4):1091-1104.
717 46. Zhang X*, et al.* (2010) Altered neurocircuitry in the dopamine transporter knockout mouse
718 brain. *PLoS One* 5(7):e11506.
719 47. Gallagher JJ, Zhang X, Ziomek GJ, Jacobs RE, & Bearer EL (2012) Deficits in axonal
720 transport in hippocampal-based circuitry and the visual pathway in APP knock-out
721 animals witnessed by manganese enhanced MRI. *Neuroimage* 60(3):1856-1866.
722 48. Gallagher JJ*, et al.* (2013) Altered reward circuitry in the norepinephrine transporter
723 knockout mouse. *PLoS One* 8(3):e57597.
724 49. Delora A*, et al.* (2016) A simple rapid process for semi-automated brain extraction from
725 magnetic resonance images of the whole mouse head. *J Neurosci Methods* 257:185-193.
726 50. Medina CS*, et al.* (2017) Hippocampal to basal forebrain transport of Mn(2+) is impaired
727 by deletion of KLC1, a subunit of the conventional kinesin microtubule-based motor.
728 *Neuroimage* 145(Pt A):44-57.
729 51. Medina CS, Manifold-Wheeler B, Gonzales A, & Bearer EL (2017) Automated
730 Computational Processing of 3-D MR Images of Mouse Brain for Phenotyping of Living
731 Animals. *Curr Protoc Mol Biol* 119:29A 25 21-29A 25 38.

732 52. Bearer EL*, et al.* (2018) Alterations of functional circuitry in aging brain and the impact of
733 mutated APP expression. *Neurobiol Aging* 70:276-290.
734 53. Bearer EL, Barto D, & Jacobs RE (2019) Imaging the evolution acute fear: Longitudinal
735 whole brain imaging in living mice of neural activity with MEMRI. *Proceedings of the*
736 *International Society for Magnetic Resonance in Medicine... Scientific Meeting and*
737 *Exhibition. International Society for Magnetic Resonance in Medicine. Scientific Meeting*
738 *and Exhibition*, (NIH Public Access).
739 54. Medina CS*, et al.* (2019) Decoupling the Effects of the Amyloid Precursor Protein From
740 Amyloid-beta Plaques on Axonal Transport Dynamics in the Living Brain. *Front Cell*
741 *Neurosci* 13:501.
742 55. Phinyomark A, Ibanez-Marcelo E, & Petri G (2017) Resting-State fMRI Functional
743 Connectivity: Big Data Preprocessing Pipelines and Topological Data Analysis. *IEEE*
744 *Transactions on Big Data* 3(4):415-428.
745 56. Flandin G & Friston K (2008) Statistical parametric mapping (SPM). *Scholarpedia*
746 3(4):6232.
747 57. Penny WD, Friston KJ, Ashburner JT, Kiebel SJ, & Nichols TE (2011) *Statistical*
748 *Parametric Mapping: The Analysis of Functional Brain Images* (Elsevier Science).
749 58. Pallast N*, et al.* (2019) Processing Pipeline for Atlas-Based Imaging Data Analysis of
750 Structural and Functional Mouse Brain MRI (AIDAmri). *Frontiers in Neuroinformatics* 13.
751 59. Fendt M, Endres T, Lowry CA, Apfelbach R, & McGregor IS (2005) TMT-induced
752 autonomic and behavioral changes and the neural basis of its processing. *Neuroscience*
753 *and biobehavioral reviews* 29(8):1145-1156.
754 60. Rosen J, Asok A, & Chakraborty T (2015) The smell of fear: innate threat of 2,5-dihydro-
755 2,4,5-trimethylthiazoline, a single molecule component of a predator odor. 9.
756 61. Gallo M*, et al.* (2019) Limited Bedding and Nesting Induces Maternal Behavior
757 Resembling Both Hypervigilance and Abuse. 13.
758 62. Matsukawa M, Yoshikawa M, Katsuyama N, Aizawa S, & Sato T (2022) The Anterior
759 Piriform Cortex and Predator Odor Responses: Modulation by Inhibitory Circuits. *Front*
760 *Behav Neurosci* 16:896525.
761 63. Matsumoto H*, et al.* (2010) Spatial Arrangement of Glomerular Molecular-Feature
762 Clusters in the Odorant-Receptor Class Domains of the Mouse Olfactory Bulb.
763 103(6):3490-3500.
764 64. Kimbrough A*, et al.* (2020) Brain-wide functional architecture remodeling by alcohol
765 dependence and abstinence. 117(4):2149-2159.

766 65. Motta SC*, et al.* (2009) Dissecting the brain's fear system reveals the hypothalamus is
767 critical for responding in subordinate conspecific intruders. *Proceedings of the National*
768 *Academy of Sciences* 106(12):4870-4875.
769 66. Greene AS, Horien C, Barson D, Scheinost D, & Constable RT (2023) Why is everyone
770 talking about brain state? *Trends Neurosci* 46(7):508-524.
771 67. Ben-Shaul Y, Katz LC, Mooney R, & Dulac C (2010) In vivo vomeronasal stimulation
772 reveals sensory encoding of conspecific and allospecific cues by the mouse accessory
773 olfactory bulb. 107(11):5172-5177.
774 68. Canteras NS (2002) The medial hypothalamic defensive system: Hodological
775 organization and functional implications. *Pharmacology Biochemistry and Behavior*
776 71(3):481-491.
777 69. Canteras NS, Chiavegatto S, Ribeiro do Valle LE, & Swanson LW (1997) Severe
778 Reduction of Rat Defensive Behavior to a Predator by Discrete Hypothalamic Chemical
779 Lesions. *Brain Research Bulletin* 44(3):297-305.
780 70. Janitzky K, D'Hanis W, Kröber A, & Schwegler H (2015) TMT predator odor activated
781 neural circuit in C57BL/6J mice indicates TMT-stress as a suitable model for
782 uncontrollable intense stress. *Brain research* 1599:1-8.
783 71. Kunwar PS*, et al.* (2015) Ventromedial hypothalamic neurons control a defensive
784 emotion state. *eLife* 4:e06633.
785 72. Pérez-Gómez A*, et al.* (2015) Innate Predator Odor Aversion Driven by Parallel Olfactory
786 Subsystems that Converge in the Ventromedial Hypothalamus. *Current Biology*
787 25(10):1340-1346.
788 73. Koob GF & Volkow ND (2016) Neurobiology of addiction: a neurocircuitry analysis. *The*
789 *lancet. Psychiatry* 3(8):760-773.
790 74. Russo SJ & Nestler EJ (2013) The brain reward circuitry in mood disorders. *Nature*
791 *Reviews Neuroscience* 14(9):609-625.
792 75. Silva BA, Gross CT, & Graff J (2016) The neural circuits of innate fear: detection,
793 integration, action, and memorization. *Learn Mem* 23(10):544-555.
794 76. Coletta L*, et al.* (2020) Network structure of the mouse brain connectome with voxel
795 resolution. 6(51):eabb7187.
796 77. Salvan P*, et al.* (2023) Serotonin regulation of behavior via large-scale neuromodulation
797 of serotonin receptor networks. *Nature Neuroscience* 26(1):53-63.
798 78. Taylor NL*, et al.* (2022) Structural connections between the noradrenergic and cholinergic
799 system shape the dynamics of functional brain networks. *NeuroImage* 260:119455.
800 79. Zerbi V*, et al.* (2019) Rapid Reconfiguration of the Functional Connectome after
801 Chemogenetic Locus Coeruleus Activation. *Neuron* 103(4):702-718.e705.

802 80. David & Adolphs R (2014) A Framework for Studying Emotions across Species. *Cell*
803 157(1):187-200.
804 81. Flavell SW, Gogolla N, Lovett-Barron M, & Zelikowsky M (2022) The emergence and
805 influence of internal states. *Neuron* 110(16):2545-2570.
806 82. Jaric I*, et al.* (2022) The rearing environment persistently modulates mouse phenotypes
807 from the molecular to the behavioural level. *PLoS Biol* 20(10):e3001837.
808 83. Jaric I*, et al.* (2024) Using mice from different breeding sites fails to improve replicability
809 of results from single-laboratory studies. *Lab Anim (NY)* 53(1):18-22.
810 84. Usui T, Macleod MR, McCann SK, Senior AM, & Nakagawa S (2021) Meta-analysis of
811 variation suggests that embracing variability improves both replicability and
812 generalizability in preclinical research. *PLoS Biol* 19(5):e3001009.
813 85. Chang C-H & Gean P-W (2019) The Ventral Hippocampus Controls Stress-Provoked
814 Impulsive Aggression through the Ventromedial Hypothalamus in Post-Weaning Social
815 Isolation Mice. *Cell Reports* 28(5):1195-1205.e1193.
816 86. Manzano Nieves G, Bravo M, & Bath KG (2023) Early life adversity ablates sex
817 differences in active versus passive threat responding in mice. *Stress*:1-32.
818 87. Lehallier B*, et al.* (2012) Brain Processing of Biologically Relevant Odors in the Awake
819 Rat, as Revealed by Manganese-Enhanced MRI. *PLoS ONE* 7(10):e48491.
820 88. Petrus E, Saar G, Daoust A, Dodd S, & Koretsky AP (2021) A hierarchy of manganese
821 competition and entry in organotypic hippocampal slice cultures. *NMR in Biomedicine*
822 34(4).
823 89. Bartelle BB, Szulc KU, Suero-Abreu GA, Rodriguez JJ, & Turnbull DH (2013) Divalent
824 metal transporter, DMT1: A novel MRI reporter protein. *Magnetic resonance in medicine*
825 70(3):842-850.
826 90. Spring S, Lerch JP, & Henkelman RM (2007) Sexual dimorphism revealed in the
827 structure of the mouse brain using three-dimensional magnetic resonance imaging.
828 *NeuroImage* 35(4):1424-1433.
829 91. Bruce MR*, et al.* (2021) Sexually dimorphic neuroanatomical differences relate to ASD-
830 relevant behavioral outcomes in a maternal autoantibody mouse model. *Molecular*
831 *Psychiatry* 26(12):7530-7537.
832 92. Holz NE*, et al.* (2023) A stable and replicable neural signature of lifespan adversity in the
833 adult brain. *Nature Neuroscience*.
834 93. Lerch JP*, et al.* (2011) Maze training in mice induces MRI-detectable brain shape
835 changes specific to the type of learning. *NeuroImage* 54(3):2086-2095.
836 94. Ashburner J*, et al.* (2012) SPM8 manual.
837 95. Ashburner J*, et al.* (2014) SPM12 manual.

96. Carter CS, Lesh TA, & Barch DM (2016) Thresholds, Power, and Sample Sizes in Clinical Neuroimaging. *Biological Psychiatry: Cognitive Neuroscience and Neuroimaging* 1(2):99-100.
97. Mumford JA (2012) A power calculation guide for fMRI studies. *Social Cognitive and Affective Neuroscience* 7(6):738-742.
98. Vandekar SN & Stephens J (2021) Improving the replicability of neuroimaging findings by thresholding effect sizes instead of p-values. 42(8):2393-2398.
99. Hammelrath L*, et al.* (2016) Morphological maturation of the mouse brain: An in vivo MRI and histology investigation. *NeuroImage* 125:144-152.
100. Brigman JL, Mathur P, Lu L, Williams RW, & Holmes A (2009) Genetic relationship between anxiety-related and fear-related behaviors in BXD recombinant inbred mice. 20(2):204-209.
101. Noldus LPJJ, Spink AJ, & Tegelenbosch RAJ (2001) EthoVision: A versatile video tracking system for automation of behavioral experiments. *Behavior Research Methods, Instruments, & Computers* 33(3):398-414.
102. Fox J & Weisberg S (2019) An R Companion to Applied Regression.
103. Lenth RV (2022) emmeans: Estimated Marginal Means, aka Least-Squares Means.
104. Pinheiro J, Bates D, & Team RC (2022) nlme: Linear and Nonlinear Mixed Effects Models.
105. Pinheiro JC & Bates DM (2000) Mixed-Effects Models in S and S-PLUS.
106. Posit t (2022) RStudio: Integrated Development Environment for R.
107. Team RC (2022) R: A Language and Environment for Statistical Computing.
108. Wickham H (2016) ggplot2: Elegant Graphics for Data Analysis.
109. Wickham H*, et al.* (2019) Welcome to the Tidyverse. 4(43):1686.
110. Tyszka JM, Readhead C, Bearer EL, Pautler RG, & Jacobs RE (2006) Statistical diffusion tensor histology reveals regional dysmyelination effects in the shiverer mouse mutant. *NeuroImage* 29(4):1058-1065.